A binding site for phosphoinositide modulation of voltage-gated sodium channels described by multiscale simulations

Yiechang Lin[*#], Elaine Tao[*#], James Champion, Ben Corry[#]

Research School of Biology, Australian National University, Canberra.

[*]*These authors contributed equally.*

[#]yiechang.lin@anu.edu.au, elaine.tao@anu.edu.au, ben.corry@anu.edu.au

Voltage gated sodium channels (Na_v) are membrane proteins which open to facilitate the inward flux of sodium ions into excitable cells. In response to stimuli, Na_v channels undergo a transition from the resting, closed state to an open state which allows ion influx, before rapidly inactivating. Dysregulation of this functional cycle due to mutations leads to diseases including epilepsy, pain conditions and cardiac disorders, making Na_v channels a significant pharmacological target. Phosphoinositides are important lipid cofactors for ion channel function. The phosphoinositide $PI(4,5)P_2$ decreases $Na_v1.4$ activity by increasing the difficulty of channel opening, accelerating fast activation and slowing recovery from fast inactivation. Using multiscale molecular dynamics simulations, we show that $PI(4,5)P_2$ binds stably to inactivated Na_v at a conserved site within the DIV S4-S5 linker, which couples the voltage sensing domain (VSD) to the pore. As the Na_v C-terminal domain is proposed to also bind here during recovery from inactivation, we hypothesise that $PI(4,5)P_2$ prolongs inactivation by competing to bind to this site. In atomistic simulations, $PI(4,5)P_2$ reduces the mobility of both the DIV S4-S5 linker and the DIII-IV linker, responsible for fast inactivation, slowing the conformational changes required for the channel to recover to the resting state. We further show that in a resting state Na_v model, phosphoinositides bind to VSD gating charges, which may anchor them and impede VSD activation. Our results provide a mechanism by which phosphoinositides alter the voltage dependence of activation and the rate of recovery from inactivation, an important step for the development of novel therapies to treat Na_v-related diseases.

Introduction

Voltage-gated sodium (Na_v) channels are critical to the regulation of brain activity, cardiac rhythm, and muscle contraction. Expressed in the membranes of excitable cells, Na_v channels respond to membrane depolarization to open a pore that facilitates the selective flow of sodium current into the cell, initiating the action potential. In mammals, the Na_v channel family consists of nine subtypes (Na_v 1.1-1.9), distributed throughout the central and peripheral nervous system, as well as in cardiac and skeletal muscle (Yu and Catterall, 2003). The $Na_v1.4$ subtype is predominantly expressed in skeletal myofibers, where it initiates muscle contraction. Genetic mutations in this subtype are associated with various motor dysfunctions, such as both hyperkalaemic and hypokalaemic periodic paralyses (Jurkat-Rott et al., 2000; Mantegazza et al., 2021; Venance et al., 2006). $Na_v1.7$ is found in peripheral sensory neurons and is responsible for nociception. Several pain disorders, such as inherited erythromelalgia and small fibre neuropathy arise from gain-of-function $Na_v1.7$ mutations (Dib-Hajj et al., 2013). Both Na_v subtypes have been investigated as promising pharmacological targets for the treatment of myopathy and pain conditions (Dib-Hajj et al., 2013; Ghovanloo et al., 2021).

Structurally, Na_v channels consist of four homologous domains (DI-DIV) arranged in a domain-swapped configuration (Fig. 1A-B). Each domain comprises of six transmembrane helices (S1-S6). The central pore domain is formed by S5, S6 helices and selectivity filter (SF), while the four peripheral voltage-sensing domains (VSDs) are formed by S1-S4 (de Lera Ruiz and Kraus, 2015; Pan et al., 2018). The pore domain also features lateral fenestrations that provide a pathway for the access of small molecules to the pore via the membrane (Gamal El-Din et al., 2018) and have been shown in computational studies to be accessible to lipid tails (Boiteux et al., 2014; Martin and Corry, 2014; Raju et al., 2013; Tao and Corry, 2022). Additionally, the C-terminal domain (CTD) extends from the DIV S6 helix into the cytoplasm, where it is thought to associate with the DIII-IV and DIV S4-S5 linkers in the resting state (Clairfeuille et al., 2019).

Na_v channels adopt distinct functional states during the cycle of membrane depolarization and repolarization (Fig. 1C). In the resting state, the pore is closed and VSD S4 helices are in the down, deactivated state. Membrane depolarization triggers the asynchronous transition of VSD I-III S4 helices to the up, activated conformation, causing Na_v channels to open (Capes et al., 2013; Cha et al., 1999; Goldschen-Ohm et al., 2013). During prolonged depolarization, VSD-IV moves upwards, causing the channels to adopt a fast inactivated state in which a three-residue (IFM) hydrophobic motif located on the intracellular linker between DIII and DIV (DIII-IV linker) allosterically closes the pore (Yan et al., 2017). The CTD is proposed to bind at the S4-S5 linker of VSD-IV and sequester the DIII-IV linker during the resting state. During fast inactivation, the CTD dissociates from VSD-IV and releases the DIII-IV linker to allow IFM binding (Clairfeuille *et al.*, 2019). Upon repolarization, the VSDs deactivate, the IFM motif disassociates, the CTD rebinds to VSD-IV and the pore returns to the resting state.

Phosphoinositides (PIPs) are important cellular signaling molecules found on the cytoplasmic leaflet of the mammalian cell membrane. They can exist in seven forms, with phosphorylation possible at one (PIP1), two (PIP2) or all three (PIP3) positions on the inositol ring, at the 3', 4' and/or 5' carbons. PIPs, particularly $PI(4,5)P_2$, featuring phosphates at the 4' and 5' carbon positions (Fig. 1D), are known to bind and modulate the activity of numerous ion channels families (Hille et al., 2015). These include voltage-gated ion channels, some of which have been resolved with $PI(4,5)P_2$ bound (Gao et al., 2021; Sun and MacKinnon, 2020). PIP is known to interact with the VSDs of different potassium channels, to stabilize the positive gating charges and support the voltage-sensing mechanism (Schmidt et al., 2006). By also binding at the VSD-pore interface in channels such as $K_v7.1$, PIP is proposed to facilitate coupling of VSD movement to pore opening (Kasimova et al., 2015; Ma et al., 2022; Sun and MacKinnon, 2020). $PI(4,5)P_2$ also forms specific interactions with VSD-II of Cav2.2 in the down-state, making channel activation more difficult (Gao *et al.*, 2021). Although $PI(4,5)P_2$ is known to bind to numerous voltage gated ion channels, its effects on channel gating and function are complex and yet to be fully elucidated.

Recent experiments show that $Na_v1.4$ channel kinetics and voltage dependence are modulated by $PI(4,5)P_2$ (Gada et al., 2023). $PI(4,5)P_2$ inhibits $Na_v1.4$ by causing a depolarizing shift in voltage dependence of activation, accelerating transition to the inactivated state and slowing recovery from inactivation, resulting in reduced peak current and suppression of late current (summarized in Fig. 1C). While this is likely to occur via a direct interaction with $Na_v1.4$, the structural basis of $PI(4,5)P_2$ modulation remains to be understood.

Here, we used a combination of coarse-grained and atomistic MD simulations to identify a putative PIP binding site to inactivated $Na_v1.4$ in VSD-IV and the DIII-IV linker. We analyze the atomistic level interactions between the positively charged residues at this site with $PI(4,5)P_2$ and PI(4)P, comparing this with structurally resolved PIP binding sites in the related ion channels $Ca_v2.2$ and $K_v7.1$. Consistent with the sequence conservation at the identified site, we find that PIPs also bind to Nav1.7 in coarse-grained simulations, with notable differences dependent on VSD conformation states. This work provides insight into how PIPs can negatively regulate Na_v channels, a first step for the potential development of PIP-analogue sodium channel inhibitors.

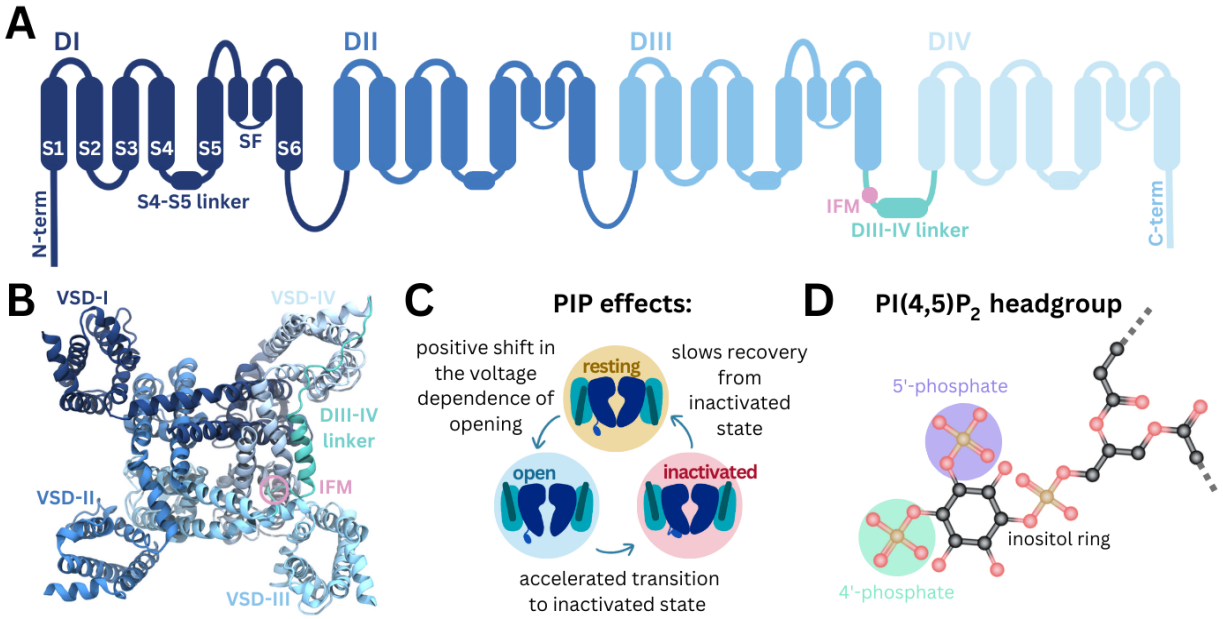

Fig. 1 Structure of Na_v and modulation by phosphoinositides (A) Na_v channel topology featuring transmembrane helices (S1-S6), the selectivity filter (SF) and the DIII-IV linker (containing the IFM motif) located between DIII and DIV. **(B)** $Na_v1.4$ structure (6agf) showing the four domain-swapped voltage sensor domains (VSDs I-IV), pore and DIII-IV linker on the intracellular side. **(C)** Summary of $PI(4,5)P_2$ effects on transitions between Na_v channel functional states (Gada *et al.*, 2023) **(D)** Structure of the $PI(4,5)P_2$ headgroup with the 4'- and 5'- phosphates indicated

Results

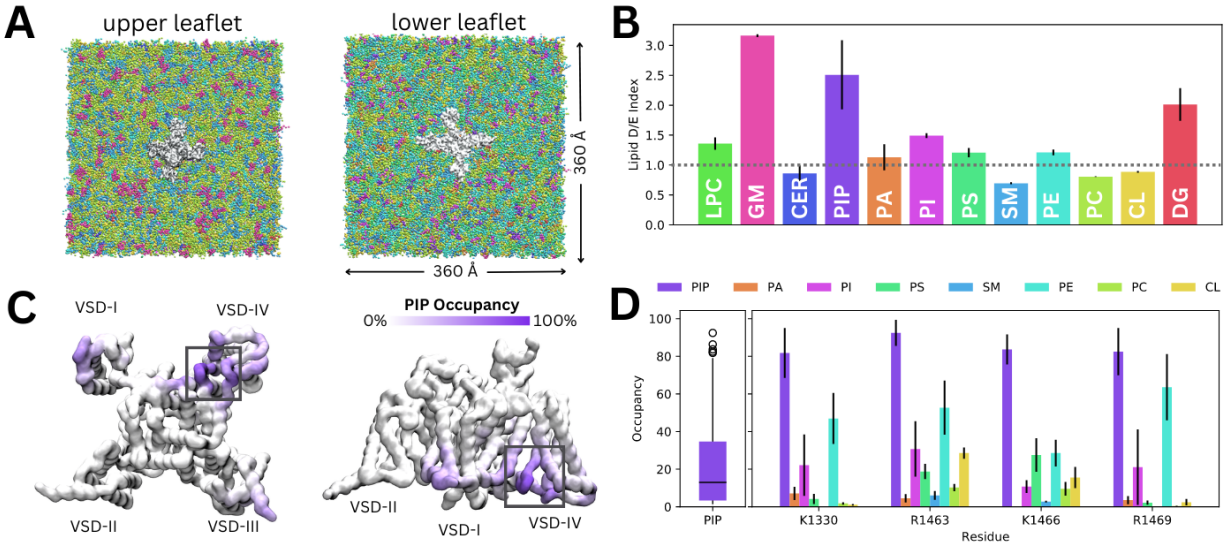

Fig. 2 Lipid fingerprint and binding of all PIP types to $Na_v1.4$ (A) $Na_v1.4$ embedded in a 360 Å x 360 Å model mammalian membrane containing 63 lipid species. **(B)** Lipid depletion enrichment index of lipids around $Na_v1.4$ grouped into 12 headgroup types **(C)** $Na_v1.4$, shown from the intracellular (left) and membrane (right) sides, colored by PIP occupancy (darker purple = greater PIP occupancy) **(D)** Distribution of PIP binding occupancies (left) and occupancy of lipid species at 4 residues with the highest PIP occupancy.

To investigate how diverse lipid species interact with $Na_v1.4$, we carried out coarse-grained simulations of $Na_v1.4$ (PDB ID: 6agf, inactivated state) embedded in a complex mammalian membrane for 16 μs in triplicate (Fig. 2A). Glycosphingolipid (GM), phosphoinositide (PIP) and diacylglycerol (DAG) were highly enriched around Nav1.4 (Fig. 2B). Additionally, we observed modest enrichment of lysophosphatidylcholine (LPC), phosphatidylinositol (PI), phosphatidylserine (PS) and phosphatidylethanolamine (PE) and slight depletion of ceramide (CER), sphingomyelin (SM), phosphatidylcholine (PC) and cholesterol (CL). To investigate specific interactions, we generated z-density maps and calculated the per-residue occupancy of the 12 different lipid types (Fig. 2C, Fig. S1-2). Binding residues of interest were identified by constructing occupancy distributions by residue for each lipid type and identifying outlying values with high occupancies (Fig. S3). DG lipids form significant interactions within the lateral fenestrations of $Na_v1.4$ (Fig. S2). LPC and PI also frequently interact with different VSD residues (Fig. S1).

Given our interest in understanding the modulation of $Na_v1.4$ by PIPs, we focus on their interactions for the remainder of this manuscript. Despite the very low concentration of PIPs (0.5% each of PIP1, PIP2 and PIP3) in the mammalian membrane, they are highly enriched around $Na_v1.4$, particularly near the DIII-IV linker and the VSD-IV (Fig. 2C). Contact analysis revealed a putative PIP binding site involving the K1330 residue of the DIII-IV linker and residues R1463, K1466 and R1469 in the DIV S4-S5 linker, which connects the pore and VSD-IV (Fig. 2D). Across all three replicates, only residues within this site were occupied by PIPs for more than 80% (Quartile 3 + 1.5 x Interquartile range) of simulation time on average (Fig. 2D). We note that these

residues have higher occupancies for PIP compared to other lipids, including other negatively charged phospholipids (PA, PS and PI) (Fig. 2D).

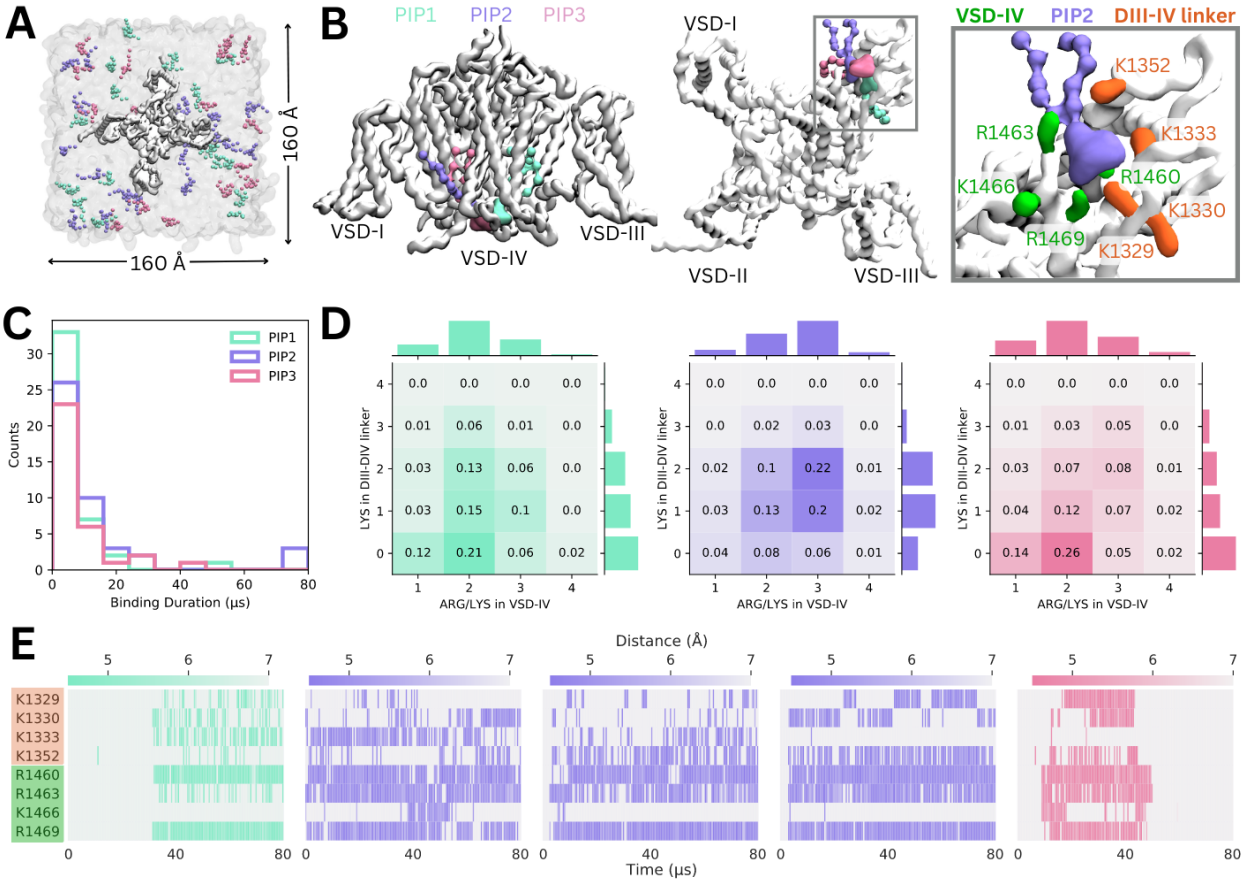

Fig. 3 Binding of different PIP species in enriched PIP simulations (A) Enriched PIP simulation system, with $Na_v1.4$ embedded in a POPC membrane (transparent gray) and 5% each of PIP1 (blue), PIP2 (purple) and PIP3 (pink) added to the lower leaflet. **(B)** Representative snapshots showing PIP binding to VSD-IV and the DIII-IV linker. $Na_v1.4$ is shown in white and PIPs are colored according to residue name (PIP1 in blue, PIP2 in purple and PIP3 in pink) **(C)** A frequency distribution showing interaction times for each PIP species, defined as the length of a continuous period in which a PIP was within 0.7 nm of two VSD IV binding site residues. **(D)** Frequency plots showing number of positive residues interacting with bound PIP in the DIII-IV linker (vertical) and VSD-IV (horizontal). **(E)** Minimum distance between binding residues on $Na_v1.4$ and bound PIPs lipid across simulation time for the 5 longest binding events, colored by distance and the type of PIP bound.

Simulations in a complex mammalian membrane showed that PIP species bind specifically and selectively to $Na_v1.4$ in the presence of other negatively charged lipids and at low, physiological concentrations. However, the large membrane required, and long PIP binding durations prevented sampling of large numbers of binding and unbinding events. To address this, we carried out additional simulations where $Na_v1.4$ was placed in a smaller POPC membrane with a 5% concentration of each PIP species in the lower leaflet (Fig. 3A).

Across ten replicates of these enriched PIP simulations, each carried out for 80 μs, we observed all three PIP species binding at the identified site on VSD-IV and DIII-IV linker (Fig. 3B). PIPs can approach and bind to this site from either side of the VSD, however, PIP1 only forms stable interactions when it approaches and binds from the VSD-I side while PIP2 and PIP3 usually bind

from the VSD-III side (Fig. 3B). These enriched PIP simulations also revealed additional positively charged residues in the DIII-IV linker (K1329, K1333 and K1352) and DIV S4 (R1460) which support binding.

There were 156 PIP binding/unbinding events with duration greater than 2 μs occurring the identified site (Fig. 3C). Of these, 43 were with PIP1, 44 with PIP2 and 33 with PIP3. The number of short-term (2-10 μs) interactions decreased with headgroup charge. That is, PIP1 formed the greatest number of short-term interactions while PIP3 had the fewest. Of the 31 binding events with duration greater than 10 μs, 7 were with PIP1, 15 with PIP2 and 9 with PIP3 (Fig. S3-4).

When we analyzed interactions occurring during 2-80+ μs binding events, we found that the number of interacting basic residues changes depending on the PIP headgroup charge (Fig. 3D). PIP1 (headgroup charge: -3e) binding is most frequently coordinated by two positive charges in VSD-IV and zero or one residue in the DIII-IV linker. PIP2 (headgroup charge: -5e) binding most frequently involves one or two interactions from the DIII-IV linker and three from VSD-IV for a total of five interactions. Interestingly, despite its greater negative charge, PIP3 (headgroup charge: -7e) has interacts similarly to PIP1, and has fewer interactions than PIP2.

The minimum distance between the interacting PIP headgroup and each binding residue across simulation time is shown for the five 40+ μs PIP binding events (Fig. 3E). Of these, three are PIP2 binding events which almost span the entire 80 μs of simulation. One 40+ μs binding event each for PIP1 and PIP3 were also observed. The stable PIP1 binding event observed involved interactions with R1460 and R1469 in VSD-IV, as well as fluctuating interactions with the four residues of the DIII-IV linker (K1329, K1330, K1333, K1352). The three long term PIP2 binding events observed were similar to each other, mainly stabilized by R1460, R1463 and R1469. As with PIP1, the number and identity of interacting DIII-IV linker residues varied across the span of each simulation and between replicates, owing to the flexibility of the linker. Like PIP2, PIP3 binding was characterized by stable interactions with R1460, R1463 and R1469 (VSD-IV) as well as K1329 and K1330 (DIII-IV linker).

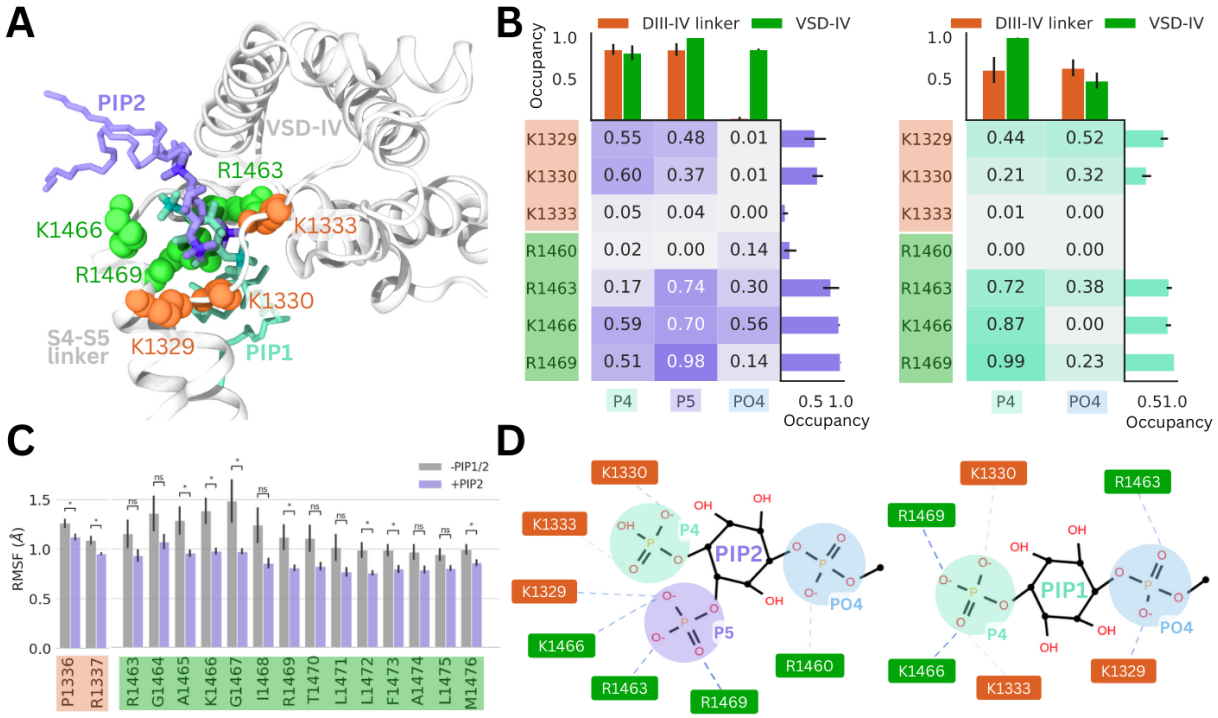

Fig. 4 PI(4,5)P_2 and PI(4)P binding to $Na_v1.4$ in atomistic simulations (A) Representative snapshots of PI(4,5)P_2 bound from the VSD-I side (purple stick) and PI(4)P bound from the VSD-III side (cyan stick), with six basic residues forming the binding site located on the DIII-IV linker (orange VDW representation) and VSD-IV S4-S5 linker (shown in green VDW representation) visualized from the intracellular face of the protein **(B)** Proportion of frames where each of the binding site residues were identified to be within 4.5 Å with the different headgroup regions, P4, P5 and PO4, for PI(4,5)P_2 (left) and PI(4)P (right) **(C)** Comparison of RMSF per carbon-alpha for simulations with and without bound PI(4,5)P_2, showing residues on the S4-S5 linker and DIV linker with significant differences in mobility (p-value < 0.05) **(D)** Interaction network plots between the PIP headgroup and basic binding residues on DIII-IV linker (orange) and DIV S4-S5 linker (green), generated by ProLIF – showing the dominant interactions across simulations of PI(4,5)P_2 and PI(4)P.

Coarse-grained simulations enhance sampling by reducing system size, enabling larger time steps and construction of a smoother energy surface. However, this loss of resolution prevents distinction between phosphate positions on the inositol group and does not permit analysis of protein conformational changes induced by PIP binding. To address this, we backmapped representative snapshots from our PIP enriched simulations, where we observed stable, long-term binding events between $Na_v1.4$ and PIP1/PIP2. The coarse-grained PIP1 and PIP2 molecules were converted to the atomistic PI(4)P and PI(4,5)P_2 respectively. For each system, 7.5 μs of atomistic simulations were performed (5 replicates, 1.5 μs each).

In these simulations, the PI(4,5)P_2 headgroup was stable at the binding site identified in coarse-grain simulations (RMSD <2.2 Å) (Fig. 4A, Fig. S6). PI(4,5)P_2 binding is predominantly coordinated by R1469 on the DIV S4-S5 linker, as well as R1466 and R1463. In one replicate, PI(4,5)P_2 associates with R1460 via the phosphate group (PO4) that connects the headgroup to the PIP tails. The PI(4,5)P_2 headgroup also forms electrostatic interactions with K1329 and K1330 in the DIII-IV linker, but forms few contacts with K1333 (Fig. 4B, Fig. S7). This loop portion of the

199 DIII-IV linker is highly flexible (Fig. S6), thus the lysine sidechains are able to flip between binding
200 the PI(4,5)P_2 headgroup and facing the intracellular space.

201 The 4'-phosphate formed interactions with residues belonging to the DIII-IV linker (K1329 and
202 K1333) and DIV S4-S5 linker (K1666 and R1469) with similar frequency, in 55-60% of simulation
203 frames (Fig. 4B). In contrast, the 5'-phosphate formed contacts with three VSD-IV S4-S5 residues
204 (R1463, K1466 and R1469) in 70-98% of simulation frames and DIII-IV linker residues in 37-48%
205 of frames. Taken together, this data suggests that although the headgroup is flexible when bound,
206 the 5'-phosphate is more important for coordinating VSD-IV S4-S5 residues while the 4'-
207 phosphate associates with both regions of the binding site.

208 Atomistic simulations of PI(4)P bound from the VSD-III side show that this is also a stable pose
209 (RMSD <2 Å), where the headgroup interacts with the same positively charged residues as seen
210 for PI(4,5)P_2 (Fig. 4A, Fig. S6). The residues on the S4-S5 linker, R1463, K1466 and R1469,
211 predominantly bind to the 4'-phosphate (Fig. 4B). Due to the more buried location of PI(4)P
212 binding, the PO4 phosphate can associate more with DIII-IV linker lysines (Fig. 4B), however, the
213 absence of the 5'-phosphate leads to a reduced number of total electrostatic interactions (Fig.
214 S8).

215 To investigate structural changes that might occur in the presence of PI(4)P/PI(4,5)P_2, we also
216 carried out simulations of the inactivated Na_v1.4 structure without any PIPs bound for comparison.
217 Although the DIII-IV linker remains bound throughout simulations both with and without PIPs,
218 residues P1336 and R1337 in the DIII-IV linker downstream of the IFM motif are significantly less
219 mobile with PI(4,5)P_2 present (Fig. 4C). Additionally, seven residues belonging to the DIV S4-S5
220 linker, including binding residues K1466 and R1469, also have significantly lower mobility when
221 PI(4,5)P_2 is bound (Fig. 4C). In the PI(4)P bound simulations, there were no significant differences
222 in DIII-IV linker or S4-S5 linker mobility.

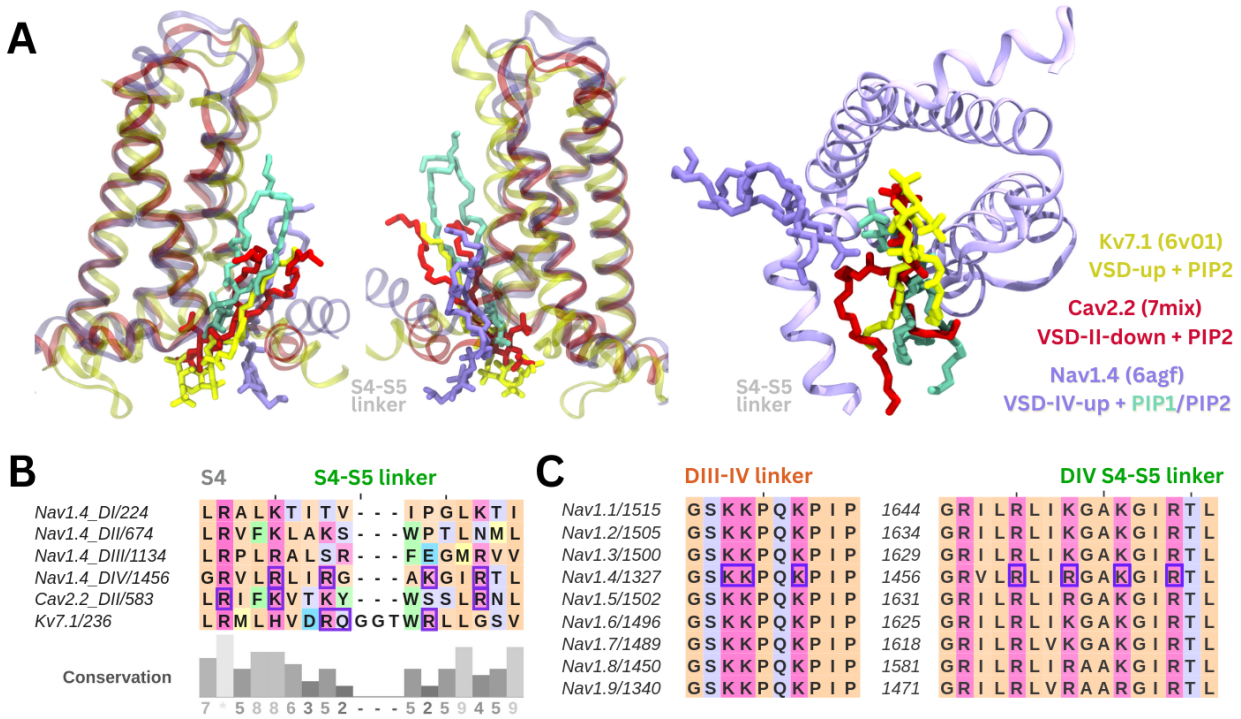

Fig. 5 Comparison of the identified phosphoinositide binding site to Na_v subtypes and other ion channels (A) Binding poses of $PI(4,5)P_2$ (in purple) and PI(4)P (in cyan) aligned with two other tetrameric channels structures $K_v7.1$ (6v01, in yellow) and $Ca_v2.2$ (7mix, in red) that were resolved with $PI(4,5)P_2$ at their respective VSDs. **(B)** Sequence alignment of the S4 helix and S4-S5 linker of the four domains of $Na_v1.4$, compared to VSD-II of $Ca_v2.2$ and one of the four identical VSDs of $K_v7.1$; residues colored by amino acid class; purple boxes indicate $PI(4,5)P_2$ binding residues (identified with 5 Å of the headgroup). **(C)** Sequence alignment of the nine human Na_v channel subtypes shows high sequence similarity in the S4 helix, S4-S5 linker and DIII-IV linker regions.

The PIP binding poses seen in our simulations is similar to resolved binding poses for $PI(4,5)P_2$ in cryo-EM structures of $Ca_v2.2$ and $K_v7.1$ (Fig. 5A). A sequence alignment of $Na_v1.4$ VSDs show that there are more positively charged residues present in the S4/S4-S5 linker regions of DIV compared to the other domains (Fig. 5B). PIP is bound at similar VSD residues on both these ion channels, with PIP forming interactions with a gating charge further up the S4 helix in $Ca_v2.2$ due to the VSD being in a different state. Additionally, the high sequence similarity in the S4/S5-S5 linker and DIII-IV linker regions between the nine human Na_v channel subtypes suggests conservation of the PIP binding site (Fig. 5C).

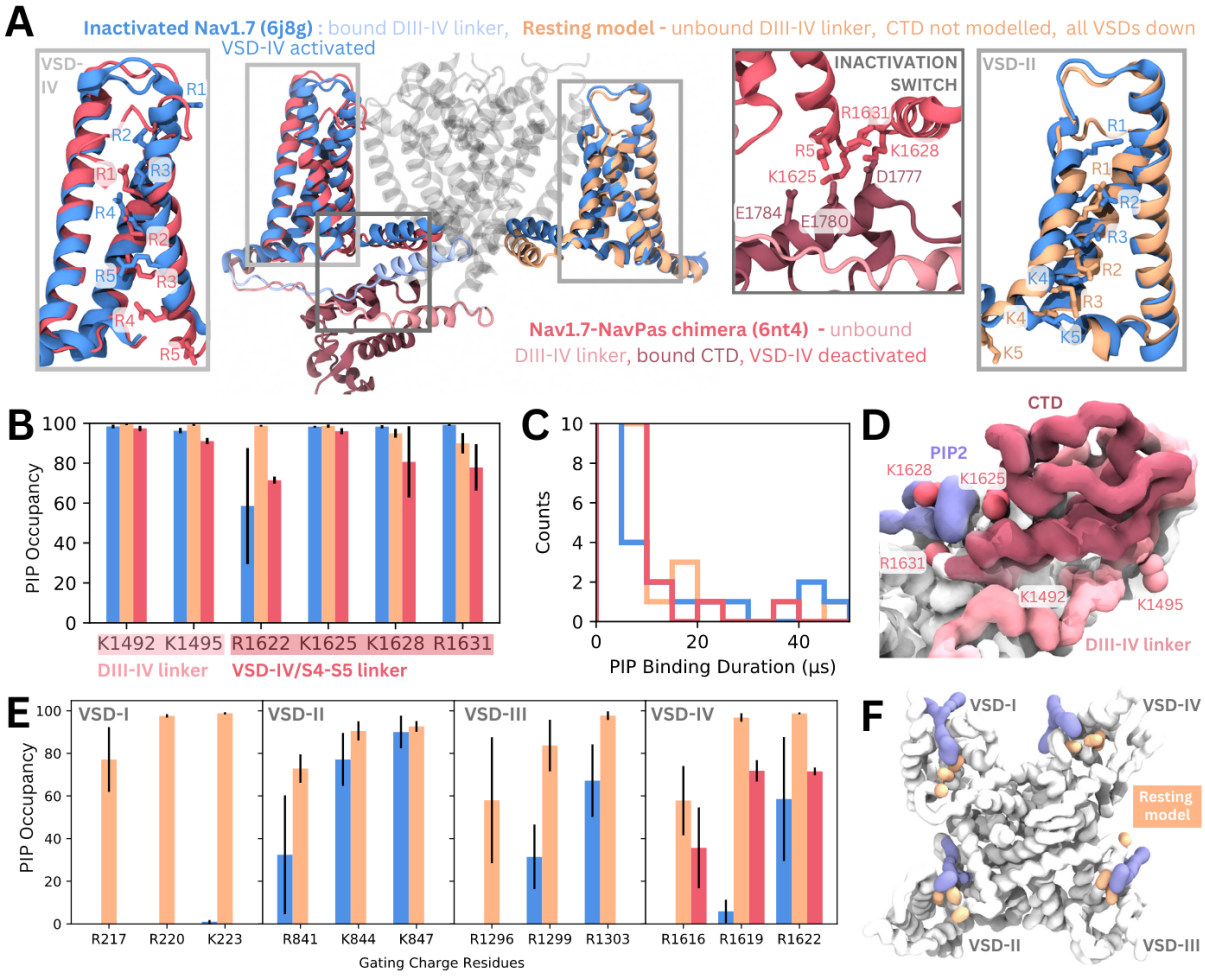

Fig. 6 PIP binding to Nav1.7 with different VSD states in coarse-grained simulations (A) Atomistic representation of the three different Nav1.7 structures simulated: (1) the inactivated state (blue, PDB ID: 6j8g) with the VSDs all in the activated, up state (2) the Nav1.7-NavPas chimera (pink, PDB ID: 6nt4) with the Nav1.7 VSD-IV in the deactivated, down state and a bound NavPas CTD (3) a Nav1.7 resting state model (orange, model generation detailed in Table. S2) with all four VSDs in the deactivated, down state. Panel insets show the different conformations of VSD-IV (left) and VSD-II (right) across different structures. The inactivation switch formed by the CTD and VSD-IV S4-S5 linker proposed by Clairfeuille et al. is shown (middle). **(B)** Occupancy of all PIPs (PIP1, PIP2, PIP3) at binding site residues in the three systems **(C)** Distribution of PIP binding durations at the identified site **(D)** Representative simulation snapshot of PIP binding at DIV S4-S5 linker in the Nav1.7-NavPas system. The CTD (dark pink) prevents PIP access to DIII-IV linker lysines **(E)** PIP occupancy at the bottom three gating charges on VSD I-III in the inactivated (blue) and resting state model (orange) simulations. For VSD-IV, PIP occupancy in the Nav1.7-NavPas system (pink) is also shown. (F) Representative simulation snapshot showing PIP (purple) binding at the gating charges (orange) in the resting state model simulations.

To assess possible state- and subtype-dependent differences in PIP binding, we performed embedded three structures of Nav1.7 with different VSD conformations in a PIP enriched membrane (Fig. 6A). The inactivated Nav1.7 structure (blue, PDB ID: 6j8g) contains all VSDs in the activated/up state and a bound DIII-IV linker. We also simulated a NavPas (American cockroach) chimera structure with a human Nav1.7 VSD-IV in the deactivated/down state (VSDs I-III are activated, and from NavPas) (pink, PDB ID: 6nt4). This structure features a dissociated DIII-IV linker and a resolved C-terminal domain bound to the DIV S4-S5 linker (forming the

260 ‘inactivation switch’) at residues identified to form part of our PIP binding site. To assess PIP
261 binding at VSD I-III in the deactivated/down state, we modelled the $Na_v1.7$ resting state based on
262 templates structures in which different VSDs have been captured in deactivated states with the
263 aid of toxins (detailed in Table S2). These structures feature three or more of the gating charge
264 residues below the hydrophobic constriction site (HCS) and displacement of the S4-S5 linker (Fig.
265 S9). Given that no resting state mammalian Na_v channel structure has been resolved, it is possible
266 that the modelled VSDs may not reflect the fully deactivated state.

267 In triplicate 50 us coarse-grained simulations, PIPs bind to the analogous site to that seen in
268 $Na_v1.4$ in the inactivated $Na_v1.7$ structure, interacting with residues belonging to both the DIII-IV
269 linker and VSD-IV for durations comparable to Nav1.4, (Fig. 6B-C, Fig. S10). Binding of PIP to
270 the DIV S4-S5 linker to the deactivated VSD-IV in the Nav1.7-NavPas chimera and resting state
271 model was also observed (Fig. 6B-C). However, in the Nav1.7-NavPas chimera, the PIP bound
272 at the S4-S5 linker cannot simultaneously associate with the DIII-IV linker (Fig. S10), due to its
273 sequestration by the C-terminal domain, which moves the lysines away from the binding VSD-IV
274 residues (Fig. 6D). Instead, K1491, K1492 and K1495 (on the DIII-IV linker) are occupied by
275 different PIPs on the other side of the VSD. In the resting state model, which features an unbound
276 DIII-IV linker PIPs binding at the DIV S4-S5 residues also do not associate with the DIII-IV linker
277 (Fig S10). Comparison of binding durations at this site across the three systems reveals a greater
278 number of long PIP interactions ($> 20\ \mu s$) with inactivated Nav1.7 (5) compared to Nav1.7-NavPas
279 (3) or the resting state model (2) where VSD-IV is down, and the DIII-IV linker is dissociated.

280 There are state-dependent differences in PIP occupancy at the gating charges in each VSD (Fig.
281 6E-F, Fig. S11). PIP can associate with the lowest three gating charges VSD-I of the resting state
282 model, but not in the inactivated state (Fig. 6E). This is likely due to the large displacement in the
283 DI-S4 helix, which moves down three helical turns in the resting state model so that all gating
284 charges are below the HCS (Fig. S9). In VSD II and III, the PIP interaction differences between
285 inactivated and resting state are present but less pronounced, owing to a smaller difference in the
286 relative displacement between the gating charges between states (Fig. S9). PIP occupancy is
287 also higher at VSD-IV when it is in the deactivated conformation, however, the presence of a
288 bound CTD in the Nav1.7-NavPas chimera reduces this.

289

290 Discussion

291 Recently, $PI(4,5)P_2$ was shown to be a negative regulator of $Na_v1.4$, modulating channel kinetics
292 and voltage dependence. Presence of $PI(4,5)P_2$ causes a depolarizing shift in the voltage
293 dependence of activation, making $Na_v1.4$ opening more difficult in a physiological context.
294 Additionally, it stabilizes the inactivated state of $Na_v1.4$, marked by both shortened inactivation
295 times and slowed recovery from the inactivation.

296 Using a multiscale simulation approach, we identified a putative PIP binding site comprised of
297 positively charged residues belonging to the S4 helix/S4-S5 linker of VSD-IV (R1460, R1463,
298 K1466, R1469) and DIII-IV linker (K1329, K1330, K1333, K1352). Coarse grained simulations of
299 $Na_v1.4$ embedded in a complex membrane showed that PIP interacts with residues belonging to
300 VSD-IV and the DIII-IV linker. In coarse grained enriched PIP simulations, PIP2 formed longer

301 duration interactions with $Na_v1.4$ than PIP1 and PIP3, supported by a greater number of charged
302 interactions. Atomistic simulations verified the stability of $PI(4,5)P_2$ (the most common PIP2
303 species in the plasma membrane) at this site and showed that the binding of $PI(4,5)P_2$ reduces
304 the mobility of some DIV S4-S5 and DIII-IV linker residues. Simulations of $Na_v1.7$ with VSDs in
305 different conformational states showed that the PIP binding site is conserved in $Na_v1.7$ and that
306 PIP interactions at VSD gating charges are functional state dependent, with more interactions
307 being formed when the VSDs are deactivated.

308 The DIII-IV linker, CTD and S4-S5 linkers all play key roles throughout the Na_v conformational
309 cycle. Mutation of the IFM inactivation motif as well as other residues in the DIII-IV linker alter fast
310 inactivation and recovery from fast inactivation (McPhee et al., 1998; West et al., 1992). While the
311 precise role of the Na_v C-terminal domain and its conformation during the Na_v activation cycle
312 remain elusive, it is likely to be important for coordinating fast inactivation (Clairfeuille *et al.*, 2019;
313 Mantegazza et al., 2001). CTD binding to DIV S4-S5 and sequestration of the DIII-IV linker is
314 proposed to occur in the resting state. After the pore opens, activation of VSD-IV is thought to
315 cause CTD dissociation, releasing the DIII-IV linker to allow fast inactivation. Residues in 'switch
316 1' of the CTD-binding site on the DIV S4-S5 stably bind PIP in our simulations of inactivated
317 Nav1.4 and Nav1.7. We hypothesize that PIP binding at this location makes it more difficult for
318 the CTD to reassociate with VSD-IV, a conformational change which is required during recovery
319 from inactivation.

320 More generally, the S4-S5 linkers in all four domains couple the VSD to the pore helices and
321 adopt different orientations depending on VSD activation states. When the VSD is activated (in
322 the open and inactivated states), the S4-S5 linkers lie parallel to the membrane. In the resting
323 state, when the voltage sensor is deactivated, the S4-S5 linkers move downward below the plane
324 of the membrane. We propose that PIP binding at the identified site could additionally stabilize
325 both the DIV S4-S5 linker and DIII-IV linker to favor the inactivated state. Although the recovery
326 from fast inactivation occurs on the order of several milliseconds (Bezanilla and Armstrong, 1977),
327 and is beyond atomistic simulation timescales, we observed statistically significant reductions in
328 the RMSF of several DIII-IV linker and DIV S4-S5 linker residues when $PI(4,5)P_2$ was bound in
329 1.5 μs atomistic simulations. Reduction in the mobility of the DIII-IV linker may slow the
330 dissociation of the upstream IFM motif and stabilization of the S4-S5 linker prevents the downward
331 movement required for the channel to transition back to the resting state.

332 The PIP binding residues identified here are conserved in $Na_v1.1$-1.9 (Fig. 5D), suggestive of a
333 shared binding site and mechanism for PIP-mediated modulation across subtypes. Mutations at
334 these conserved residues in other subtypes lead to various gain-of-function diseases (Table S1).
335 For example, analogous to the $Na_v1.4$ R1469 residue, the R1642C mutation (in $Na_v1.3$) leads to
336 developmental epileptic encepahlopathy (Zaman et al., 2018), and R1644C/H mutations (in
337 $Na_v1.5$) cause cardiac arrythmias (Frustaci et al., 2005). These diseases are associated with
338 accelerated rates of channel recovery from inactivation, consistent with our observations that an
339 interaction between $PI(4,5)P_2$ and the residue corresponding to R1469 in other Na_v subtypes
340 could be important for prolonging the fast-inactivated state.

341 The PIP binding site identified here harbors sequence and structural similarity to $PI(4,5)P_2$ binding
342 sites found in other cation channels (Fig. 5B). For example, $PI(4,5)P_2$ is resolved at a similar site
343 near the VSD and S4-S5 linker in a recent cryo-EM structure of $K_v7.1$, where the phosphate

headgroup forms analogous contacts to R249 and R243 (PDB ID: 6v01) (Sun and MacKinnon, 2020). Despite differences in the role of PI(4,5)P_2, which negatively regulates Na_v1.4 but is required for K_v7.1 pore opening, the binding site appears to be conserved. Based on the PI(4,5)P_2 binding site, a structurally similar compound was developed as an activator of K_v7 channels and proposed to be a future antiarrhythmic therapy (Liu et al., 2020).

PI(4,5)P_2 also binds to the down, deactivated state of VSD-II in Ca_v2.2 (PDB ID: 7mix) (Gao *et al.*, 2021). In this structure, the PI(4,5)P_2 headgroup interacts with two VSD-II gating charges, R584 and K587. Compared to the positioning of PI(4,5)P_2 in our simulations of Na_v1.4 with an activated VSD-IV, the headgroup associates further up the S4 helix in Ca_v2.2 due to the VSD being in a deactivated state. This is also seen in K_v7.1 which contains an extended GGT loop in the S4-S5 linker which prevents PI(4,5)P_2 binding in the VSD-down state (Mandala and MacKinnon, 2023). In our coarse-grained simulations of the resting Na_v1.7 model, we observe a similar state-dependent difference in PI(4,5)P_2 interactions with the deactivated states of each VSD. Since activation of VSDs I-III are known to be coupled to channel opening [], we propose that PIP binding at these VSDs impedes their ability to activate and thus increases the voltage threshold required of opening.

The leftward shift in voltage dependence of inactivation is less pronounced when PI(4,5)P_2 is converted to PI(4)P rather than completely dephosphorylated to PI (Gada *et al.*, 2023). This suggests that PI(4)P may play a compensatory role when PI(4,5)P_2 is not present. This is supported by our simulations which show that PI(4)P can also stably occupy the identified binding site, albeit with shorter duration and form less electrostatic interactions compared to PI(4,5)P_2. Our atomistic simulations also showed that the 5'-phosphate is more important than the 4'-phosphate for forming interactions with the DIV S4-S5 linker residues of the inactivation switch. These factors might suggest that PI(4,5)P_2 binding is preferred over PI(4)P at this site and can better compete to bind over the CTD, suggesting that PI(4,5)P_2 is more effective at stabilizing the inactivated state and preventing recovery to the resting state.

Simulations using the Martini2.2 forcefield have previously been used to investigate lipid-protein interactions and successfully predict specific lipid binding sites, including the PIP binding site on Kir channels (Stansfeld et al., 2009). While Martini2.2 simulations explicitly represent all three PIP species (PIP1, PIP2 and PIP3) present in the mammalian membrane, it does not distinguish between phosphate positions within each charge state (e.g. PI(3,4)P_2 vs PI(4,5)P_2). In this work, we employed atomistic interactions to complement and strengthen findings from coarse grain simulations, allowing us to identify the specific contribution of each PI(4,5)P_2 phosphate group to binding as well as investigate the conformational changes associated with PI(4,5)P_2 binding.

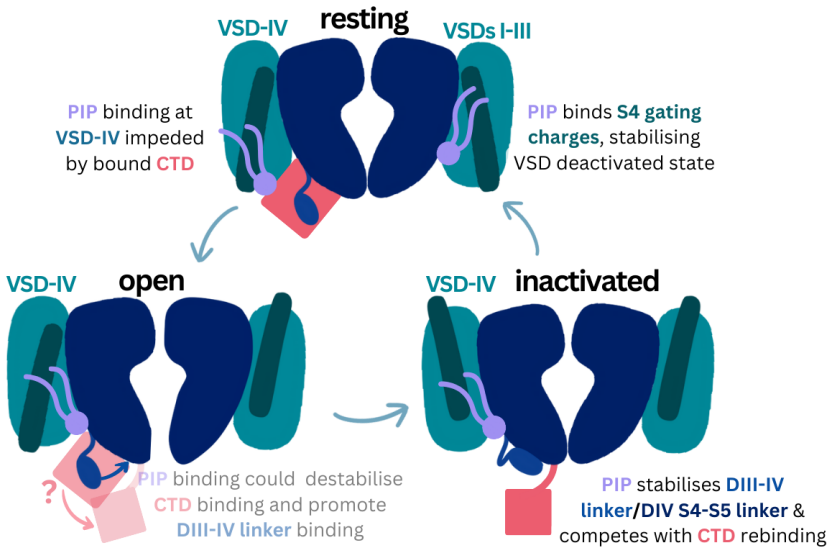

Fig. 7 Proposed mechanism of PIP effects on the sodium channel functional cycle

Conclusion

Using multiscale simulations, we show that PI(4,5)P_2 binds stably to inactivated structures of Nav1.4 and Nav1.7 at a conserved site within the DIV S4-S5 linker. As the CTD is proposed to also bind here during recovery from inactivation, we hypothesize that PI(4,5)P_2 competes with the CTD to bind to this site, prolonging inactivation. At this site, PI(4,5)P_2 simultaneously binds to the DIII-IV linker which is responsible for allosterically blocking the pore during fast inactivation (Fig. 7). Its binding reduces the mobility of both the DIV S4-S5 and DIII-IV linkers, potentially slowing the conformational changes required for the channel to recover to the resting state. We also propose that in the resting state, PIPs form additional interactions with S4 gating charges, particularly in VSD-1, anchoring them to the membrane in a way which may make the upwards movement required for their activation more difficult. Our results provide insight into how sodium channels are modulated by phosphoinositides, an important step for the development of novel therapies to treat Nav-related diseases.

Methods

Coarse grained simulations

Coarse-grained simulations of $Na_v1.4$ embedded in a complex mammalian membrane were carried out to investigate lipid-protein interactions. The inactivated $Na_v1.4$ alpha subunit (PDB ID: 6agf) (Pan *et al.*, 2018) was coarse-grained using the CHARMM-GUI Martini Maker (Jo et al., 2008; Qi et al., 2015) and embedded in a 360 Å x 360 Å complex membrane using insane.py (Wassenaar et al., 2015). The composition of the complex mammalian membrane is as reported in Ingólfsson et al. (2017). Three replicate simulations, each with different starting coordinates, were carried out for 16 μs each.

To better sample binding events, we also carried out PIP-enriched simulations in which $Na_v1.4$ was embedded in a 160 Å x 160 Å POPC membrane with 5% of each PIP species (PIP1, PIP2, PIP3) added to the cytoplasmic leaflet using insane.py. Ten replicate simulations, each with different starting coordinates, were carried out for 80 μs each.

To explore possible state and subtype dependent differences in PIP binding, the inactivated $Na_v1.7$ structure (PDB ID: 6j8g) (Shen et al., 2019) and the $Na_v1.7$-NavPas chimera with CTD bound and VSD-IV in the deactivated state (PDB ID: 6nt4) (Clairfeuille *et al.*, 2019) were also coarse-grained and simulated in PIP-enriched membranes (same protocol as above) for three replicates of 50 μs each. Additionally, a model $Na_v1.7$ with all four VSDs in the deactivated state using Modeller (Šali and Blundell, 1993). The template and structural information for this model are detailed in Table S2. In brief, VSD-I down was modelled from 7xve (Huang et al., 2022), VSD-II and VSD-III were both modelled from the deactivated VSD-II from 7k48 (Wisedchaisri et al., 2021), and VSD-IV and the unbound DIII-IV linker were modelled from the corresponding regions in 6nt4 (Clairfeuille *et al.*, 2019). Adjacent S5/S6 regions to each VSD were also modelled from each specified template to ensure proper contacts between the pore domain and VSDs. The CTD was not included in the model.

All systems were solvated and ionized with 150 mM NaCl. All coarse-grained simulations were carried out with GROMACS 2022 (Bauer et al., 2023) using the Martini2.2 forcefield (de Jong et al., 2013). Energy minimization was carried out on each system using the steepest descent method for 1,000 steps. Following this, equilibration in the constant pressure, constant volume (NVT) ensemble at 1 atm for 10 ps was carried out with backbone position restraints (1,000 kJ $mol^{-1}nm^{-2}$) using a 2-fs timestep. Following this, constant pressure and temperature (NPT) equilibration simulations were carried out, using 5-, 10-, and 20-fs timesteps in sequence, with each running for 5,000 steps. 1 atm pressure was maintained using a Berendsen barostat with semi-isotropic conditions. Production simulations were carried out in the NPT ensemble, kept at a temperature of 310 K using the Nose-Hoover thermostat (Evans and Holian, 1985) and a pressure of 1 bar using the Parrinello-Rahman barostat (Parrinello and Rahman, 1981). A time step of 20 fs was used. During production simulations, the backbone beads were weakly restrained to their starting coordinates using a force constant of 10 kJ $mol^{-1}nm^{-2}$.

Atomistic simulations

Atomistic simulations were performed to characterize atomic interactions between $Na_v1.4$ residues and the bound $PI(4,5)P_2$ headgroup. Frames from a stable PIP2 binding event (from replicate 1 of enriched PIP simulations) were clustered using a selection of the bound PIP2 headgroup beads (C1 C2 C3 PO4 P1 P2) and binding residues K1329, K1330, K1333, K1463, K1466 and R1469 with an RMSD cutoff of 2.5 Å. The protein and bound PIP2 were extracted from the representative frame of the cluster and backbone beads of the coarse-grained VSD-IV were aligned to the corresponding carbon-alpha atoms in the original cryo-EM structure of $Na_v1.4$ (Pan *et al.*, 2018). PIP2 was backmapped to atomistic coordinates of SAPI24 (the CHARMM lipid for $PI(4,5)P_2$ with protonation at the 4-position phosphate) and the protein was replaced with the 6agf structure. The system was embedded in a 140 Å x 140 Å POPC membrane, solvated and 0.15 M NaCl added using the CHARMM-GUI Membrane Builder (Jo *et al.*, 2008; Lee et al., 2016; Wu et al., 2014). An identical system was set up with $Na_v1.4$ in a POPC membrane without PIP.

Atomistic simulations were performed with Amber20 (Case et al., 2020), using the CHARMM36m (Huang et al., 2017) and TIP3P water (Jorgensen et al., 1983) forcefields. Equilibration steps were performed (minimisation, heating, pressurising), with 5 kJ/mol restraints on the protein backbone, followed by 24 ns of gradually reducing restraints. Five replicates of unrestrained production equilibrium simulations were performed, run for 1.5 μs each. The temperature was set at 310 K using the Langevin thermostat (Loncharich et al., 1992) and at a collision frequency of 5 ps^{-1}. Pressure was set at 1 bar using the Monte Carlo barostat (Åqvist et al., 2004) with anisotropic scaling and relaxation time of 1 ps. 12 Å van der Waals cut-off and hydrogen bond SHAKE constraints were used. Hydrogen mass repartitioning was used to enable a 4 fs timestep (Hopkins et al., 2015).

Analysis

Simulations were visualised and protein image figures produced using Visual Molecular Dynamics (VMD) (Humphrey et al., 1996).

Coarse grain lipid-protein interactions were characterized using in-house python scripts which used the numpy, MDAnalysis (Michaud-Agrawal et al., 2011) and pandas libraries (as done previously in Lin et al. (2022)). A cut-off of 0.7 nm was used to define interactions between lipids and protein residues. Distance heatmaps were generated based on the minimum distance between a PIP bead and the side chain (SC2) bead of the arginine or lysine residue interacting. Binding durations were calculated by first counting the number of interactions between each PIP and VSD-IV binding residues (R1460, R1463, K1466 and R1469). A binding event is defined as the time between the first and last time that PIP interacts with two or more binding residues on VSD-IV, provided that it interacts with a minimum of one binding residue between this period.

For atomistic simulations, MDAnalysis (Michaud-Agrawal *et al.*, 2011) was used to calculate RMSD of various parts of the protein and PIP headgroup, and RMSF of the carbon-alphas. Statistical significance in RMSF was assessed using student's t-test. ProLIF (Bouysset and Fiorucci, 2021) was used to compute electrostatic interactions between the protein and binding residues. Representative snapshot of PIP2 binding was generated using the WMC Clustering Tool in VMD to identify the top cluster of the PIP2 headgroup (RMSD cutoff of 3 Å), then subsequently cluster the six binding residues to identify the most representative binding configuration. Trajectories were strided every 1 ns and the first 250 ns of simulations was discarded as equilibration time for analyses of RMSF, ProLIF interactions and clustering.

ClustalOmega (Goujon et al., 2010; Sievers et al., 2011) and JalView (Waterhouse et al., 2009) were used to generate and visualize sequence alignments. Structural representations of $K_v7.1$, $Ca_v2.2$ and $Na_v1.4$ structures were created in VMD by aligning each of the S4 helices on the VSD where the PIP was bound.

Acknowledgements

This research was undertaken with the assistance of resources and services from the National Computational Infrastructure (NCI), which is supported by the Australian Government. This research is also supported by Australian Government Research Training Program (RTP) Scholarships. Y.L. is supported by a 2023 NCI HPC-AI Talent Program Scholarship.

References

Åqvist, J., Wennerström, P., Nervall, M., Bjelic, S., and Brandsdal, B.O. (2004). Molecular dynamics simulations of water and biomolecules with a Monte Carlo constant pressure algorithm. Chemical physics letters *384*, 288-294.

Bauer, P., Hess, B., and Lindahl, E. (2023). GROMACS 2022.5 Manual (2022.5).

Bezanilla, F., and Armstrong, C.M. (1977). Inactivation of the sodium channel. I. Sodium current experiments. The Journal of general physiology *70*, 549.

Boiteux, C., Vorobyov, I., and Allen, T.W. (2014). Ion conduction and conformational flexibility of a bacterial voltage-gated sodium channel. Proceedings of the National Academy of Sciences *111*, 3454-3459.

Bouysset, C., and Fiorucci, S. (2021). ProLIF: a library to encode molecular interactions as fingerprints. Journal of Cheminformatics *13*, 1-9.

Capes, D.L., Goldschen-Ohm, M.P., Arcisio-Miranda, M., Bezanilla, F., and Chanda, B. (2013). Domain IV voltage-sensor movement is both sufficient and rate limiting for fast inactivation in sodium channels. Journal of General Physiology *142*, 101-112.

Case, D.A., Belfon, K., Ben-Shalom, I.Y., Brozell, S.R., Cerutti, D.S., T.E. Cheatham, I., Cruzeiro, V.W.D., Darden, T.A., Duke, R.E., Giambasu, G., et al. (2020). AMBER 2020.

Cha, A., Ruben, P.C., George, A.L., Fujimoto, E., and Bezanilla, F. (1999). Voltage sensors in domains III and IV, but not I and II, are immobilized by Na+ channel fast inactivation. Neuron *22*, 73-87.

Clairfeuille, T., Cloake, A., Infield, D.T., Llongueras, J.P., Arthur, C.P., Li, Z.R., Jian, Y., Martin-Eauclaire, M.-F., Bougis, P.E., and Ciferri, C. (2019). Structural basis of α-scorpion toxin action on Nav channels. Science *363*, eaav8573.

de Jong, D.H., Singh, G., Bennett, W.D., Arnarez, C., Wassenaar, T.A., Schafer, L.V., Periole, X., Tieleman, D.P., and Marrink, S.J. (2013). Improved parameters for the martini coarse-grained protein force field. Journal of chemical theory and computation *9*, 687-697.

de Lera Ruiz, M., and Kraus, R.L. (2015). Voltage-Gated Sodium Channels: Structure, Function, Pharmacology, and Clinical Indications. Journal of Medicinal Chemistry *58*, 7093-7118. 10.1021/jm501981g.

Dib-Hajj, S.D., Yang, Y., Black, J.A., and Waxman, S.G. (2013). The NaV1. 7 sodium channel: from molecule to man. Nature Reviews Neuroscience *14*, 49-62.

Evans, D.J., and Holian, B.L. (1985). The nose–hoover thermostat. The Journal of chemical physics *83*, 4069-4074.

Frustaci, A., Priori, S.G., Pieroni, M., Chimenti, C., Napolitano, C., Rivolta, I., Sanna, T., Bellocci, F., and Russo, M.A. (2005). Cardiac histological substrate in patients with clinical phenotype of Brugada syndrome. Circulation *112*, 3680-3687.

Gada, K.D., Kamuene, J.M., Chandrashekar, A., Kissell, R.C., Yauch, A.K., and Plant, L.D. (2023). PI (4, 5) P2 regulates the gating of NaV1. 4 channels. Journal of General Physiology *155*, e202213255.

Gamal El-Din, T.M., Lenaeus, M.J., Zheng, N., and Catterall, W.A. (2018). Fenestrations control resting-state block of a voltage-gated sodium channel. Proceedings of the National Academy of Sciences *115*, 13111-13116.

Gao, S., Yao, X., and Yan, N. (2021). Structure of human Cav2. 2 channel blocked by the painkiller ziconotide. Nature *596*, 143-147.

Ghovanloo, M.-R., Choudhury, K., Bandaru, T.S., Fouda, M.A., Rayani, K., Rusinova, R., Phaterpekar, T., Nelkenbrecher, K., Watkins, A.R., and Poburko, D. (2021). Cannabidiol inhibits the skeletal muscle Nav1. 4 by blocking its pore and by altering membrane elasticity. Journal of General Physiology *153*, e202012701.

532 Goldschen-Ohm, M.P., Capes, D.L., Oelstrom, K.M., and Chanda, B. (2013). Multiple pore conformations
533 driven by asynchronous movements of voltage sensors in a eukaryotic sodium channel. Nature
534 communications *4*, 1350.
535 Goujon, M., McWilliam, H., Li, W., Valentin, F., Squizzato, S., Paern, J., and Lopez, R. (2010). A new
536 bioinformatics analysis tools framework at EMBL–EBI. Nucleic acids research *38*, W695-W699.
537 Hille, B., Dickson, E.J., Kruse, M., Vivas, O., and Suh, B.-C. (2015). Phosphoinositides regulate ion
538 channels. Biochimica Et Biophysica Acta (BBA)-Molecular and Cell Biology of Lipids *1851*, 844-856.
539 Hopkins, C.W., Le Grand, S., Walker, R.C., and Roitberg, A.E. (2015). Long-time-step molecular dynamics
540 through hydrogen mass repartitioning. Journal of chemical theory and computation *11*, 1864-1874.
541 Huang, G., Wu, Q., Li, Z., Jin, X., Huang, X., Wu, T., Pan, X., and Yan, N. (2022). Unwinding and spiral
542 sliding of S4 and domain rotation of VSD during the electromechanical coupling in Nav1. 7. Proceedings
543 of the National Academy of Sciences *119*, e2209164119.
544 Huang, J., Rauscher, S., Nawrocki, G., Ran, T., Feig, M., De Groot, B.L., Grubmüller, H., and MacKerell Jr,
545 A.D. (2017). CHARMM36m: an improved force field for folded and intrinsically disordered proteins.
546 Nature methods *14*, 71-73.
547 Humphrey, W., Dalke, A., and Schulten, K. (1996). VMD: visual molecular dynamics. Journal of molecular
548 graphics *14*, 33-38.
549 Ingólfsson, H.I., Carpenter, T.S., Bhatia, H., Bremer, P.-T., Marrink, S.J., and Lightstone, F.C. (2017).
550 Computational lipidomics of the neuronal plasma membrane. Biophysical journal *113*, 2271-2280.
551 Jo, S., Kim, T., Iyer, V.G., and Im, W. (2008). CHARMM-GUI: a web-based graphical user interface for
552 CHARMM. Journal of computational chemistry *29*, 1859-1865.
553 Jorgensen, W.L., Chandrasekhar, J., Madura, J.D., Impey, R.W., and Klein, M.L. (1983). Comparison of
554 simple potential functions for simulating liquid water. The Journal of chemical physics *79*, 926-935.
555 Jurkat-Rott, K., Mitrovic, N., Hang, C., Kouzmenkine, A., Iaizzo, P., Herzog, J., Lerche, H., Nicole, S., Vale-
556 Santos, J., and Chauveau, D. (2000). Voltage-sensor sodium channel mutations cause hypokalemic
557 periodic paralysis type 2 by enhanced inactivation and reduced current. Proceedings of the National
558 Academy of Sciences *97*, 9549-9554.
559 Kasimova, M.A., Zaydman, M.A., Cui, J., and Tarek, M. (2015). PIP2-dependent coupling is prominent in
560 Kv7. 1 due to weakened interactions between S4-S5 and S6. Scientific reports *5*, 1-9.
561 Lee, J., Cheng, X., Swails, J.M., Yeom, M.S., Eastman, P.K., Lemkul, J.A., Wei, S., Buckner, J., Jeong, J.C.,
562 and Qi, Y. (2016). CHARMM-GUI input generator for NAMD, GROMACS, AMBER, OpenMM, and
563 CHARMM/OpenMM simulations using the CHARMM36 additive force field. Journal of chemical theory
564 and computation *12*, 405-413.
565 Lin, Y.C., Buyan, A., and Corry, B. (2022). Characterizing the lipid fingerprint of the mechanosensitive
566 channel Piezo2. Biophysical Journal *121*, 369a.
567 Liu, Y., Xu, X., Gao, J., Naffaa, M.M., Liang, H., Shi, J., Wang, H.Z., Yang, N.-D., Hou, P., and Zhao, W.
568 (2020). A PIP2 substitute mediates voltage sensor-pore coupling in KCNQ activation. Communications
569 biology *3*, 385.
570 Loncharich, R.J., Brooks, B.R., and Pastor, R.W. (1992). Langevin dynamics of peptides: The frictional
571 dependence of isomerization rates of N-acetylalanyl-N'-methylamide. Biopolymers: Original Research on
572 Biomolecules *32*, 523-535.
573 Ma, D., Zhong, L., Yan, Z., Yao, J., Zhang, Y., Ye, F., Huang, Y., Lai, D., Yang, W., and Hou, P. (2022).
574 Structural mechanisms for the activation of human cardiac KCNQ1 channel by electro-mechanical
575 coupling enhancers. Proceedings of the National Academy of Sciences *119*, e2207067119.
576 Mandala, V.S., and MacKinnon, R. (2023). The membrane electric field regulates the PIP2-binding site to
577 gate the KCNQ1 channel. Proceedings of the National Academy of Sciences *120*, e2301985120.
578 Mantegazza, M., Cestèle, S., and Catterall, W.A. (2021). Sodium channelopathies of skeletal muscle and
579 brain. Physiological Reviews *101*, 1633-1689.

580 Mantegazza, M., Yu, F.H., Catterall, W.A., and Scheuer, T. (2001). Role of the C-terminal domain in
581 inactivation of brain and cardiac sodium channels. Proceedings of the National Academy of Sciences *98*,
582 15348-15353.
583 Martin, L.J., and Corry, B. (2014). Locating the route of entry and binding sites of benzocaine and
584 phenytoin in a bacterial voltage gated sodium channel. PLoS computational biology *10*, e1003688.
585 McPhee, J.C., Ragsdale, D.S., Scheuer, T., and Catterall, W.A. (1998). A critical role for the S4-S5
586 intracellular loop in domain IV of the sodium channel α-subunit in fast inactivation. Journal of Biological
587 Chemistry *273*, 1121-1129.
588 Michaud-Agrawal, N., Denning, E.J., Woolf, T.B., and Beckstein, O. (2011). MDAnalysis: a toolkit for the
589 analysis of molecular dynamics simulations. Journal of computational chemistry *32*, 2319-2327.
590 Pan, X., Li, Z., Zhou, Q., Shen, H., Wu, K., Huang, X., Chen, J., Zhang, J., Zhu, X., and Lei, J. (2018).
591 Structure of the human voltage-gated sodium channel Nav1. 4 in complex with β1. Science *362*,
592 eaau2486.
593 Parrinello, M., and Rahman, A. (1981). Polymorphic transitions in single crystals: A new molecular
594 dynamics method. Journal of Applied physics *52*, 7182-7190.
595 Qi, Y., Ingólfsson, H.I., Cheng, X., Lee, J., Marrink, S.J., and Im, W. (2015). CHARMM-GUI martini maker
596 for coarse-grained simulations with the martini force field. Journal of chemical theory and computation
597 *11*, 4486-4494.
598 Raju, S., Barber, A.F., LeBard, D.N., Klein, M.L., and Carnevale, V. (2013). Exploring volatile general
599 anesthetic binding to a closed membrane-bound bacterial voltage-gated sodium channel via
600 computation. PLoS computational biology *9*, e1003090.
601 Šali, A., and Blundell, T.L. (1993). Comparative protein modelling by satisfaction of spatial restraints.
602 Journal of molecular biology *234*, 779-815.
603 Schmidt, D., Jiang, Q.-X., and MacKinnon, R. (2006). Phospholipids and the origin of cationic gating
604 charges in voltage sensors. Nature *444*, 775-779.
605 Shen, H., Liu, D., Wu, K., Lei, J., and Yan, N. (2019). Structures of human Nav1. 7 channel in complex with
606 auxiliary subunits and animal toxins. Science *363*, 1303-1308.
607 Sievers, F., Wilm, A., Dineen, D., Gibson, T.J., Karplus, K., Li, W., Lopez, R., McWilliam, H., Remmert, M.,
608 and Söding, J. (2011). Fast, scalable generation of high-quality protein multiple sequence alignments
609 using Clustal Omega. Molecular systems biology *7*, 539.
610 Stansfeld, P.J., Hopkinson, R., Ashcroft, F.M., and Sansom, M.S. (2009). PIP2-binding site in Kir channels:
611 definition by multiscale biomolecular simulations. Biochemistry *48*, 10926-10933.
612 Sun, J., and MacKinnon, R. (2020). Structural basis of human KCNQ1 modulation and gating. Cell *180*,
613 340-347. e349.
614 Tao, E., and Corry, B. (2022). Characterizing fenestration size in sodium channel subtypes and their
615 accessibility to inhibitors. Biophysical Journal *121*, 193-206.
616 Venance, S.L., Cannon, S., Fialho, D., Fontaine, B., Hanna, M., Ptacek, L., Tristani-Firouzi, M., Tawil, R.,
617 and Griggs, R. (2006). The primary periodic paralyses: diagnosis, pathogenesis and treatment. Brain *129*,
618 8-17.
619 Wassenaar, T.A., Ingólfsson, H.I., Bockmann, R.A., Tieleman, D.P., and Marrink, S.J. (2015).
620 Computational lipidomics with insane: a versatile tool for generating custom membranes for molecular
621 simulations. Journal of chemical theory and computation *11*, 2144-2155.
622 Waterhouse, A.M., Procter, J.B., Martin, D.M., Clamp, M., and Barton, G.J. (2009). Jalview Version 2—a
623 multiple sequence alignment editor and analysis workbench. Bioinformatics *25*, 1189-1191.
624 West, J.W., Patton, D.E., Scheuer, T., Wang, Y., Goldin, A.L., and Catterall, W.A. (1992). A cluster of
625 hydrophobic amino acid residues required for fast Na (+)-channel inactivation. Proceedings of the
626 National Academy of Sciences *89*, 10910-10914.

627 Wisedchaisri, G., Tonggu, L., El-Din, T.M.G., McCord, E., Zheng, N., and Catterall, W.A. (2021). Structural
628 basis for high-affinity trapping of the NaV1. 7 channel in its resting state by tarantula toxin. Molecular
629 cell *81*, 38-48. e34.
630 Wu, E.L., Cheng, X., Jo, S., Rui, H., Song, K.C., Dávila-Contreras, E.M., Qi, Y., Lee, J., Monje-Galvan, V., and
631 Venable, R.M. (2014). CHARMM-GUI membrane builder toward realistic biological membrane
632 simulations. Wiley Online Library.
633 Yan, Z., Zhou, Q., Wang, L., Wu, J., Zhao, Y., Huang, G., Peng, W., Shen, H., Lei, J., and Yan, N. (2017).
634 Structure of the Nav1. 4-β1 complex from electric eel. Cell *170*, 470-482. e411.
635 Yu, F.H., and Catterall, W.A. (2003). Overview of the voltage-gated sodium channel family. Genome
636 biology *4*, 1-7.
637 Zaman, T., Helbig, I., Božović, I.B., DeBrosse, S.D., Bergqvist, A.C., Wallis, K., Medne, L., Maver, A.,
638 Peterlin, B., and Helbig, K.L. (2018). Mutations in SCN3A cause early infantile epileptic encephalopathy.
639 Annals of neurology *83*, 703-717.

640